HiSST: 3rd International Conference on High-Speed Vehicle Science & Technology

14–19 April 2024, Busan, Korea

CEAS Council of European Aerospace Societies

# Performance of a Transpiration-Cooled Sharp Leading Edge for Hypersonic Flight

*Raghul Ravichandran*[1], *Luke Doherty*[1], *Matthew McGilvray*[1]

## Abstract

This paper presents the development of a numerical tool used for the modelling and feasibility assessment of using transpiration cooling in the context of active thermal protection systems for hypersonic sharp leading edges. The finite element solver, *COMSOL Multiphysics*, is used to solve the 2D coupled partial differential equations that describe the heat transfer processes and distribution of coolant through the porous leading edge. Coolant distribution is targeted by adjusting the injector wall thickness along the leading edge. The steady-state solver is applied to a series of vehicle flight conditions and materials to consider where a transpiration-cooled leading edge may be beneficial over a passive thermal protection system. The results show that the operating regime of a transpiration cooled leading edge will be influenced by the effects of boundary layer blowoff due to excessive mass flux. Compared to an insulating C/C-SiC leading edge, the high operating temperature and conductivity of a tungsten leading edge with transpiration cooling permits operation at higher velocities and lower altitudes. However, a cooled leading edge made from Inconel is only able to operate past a passive C/C-SiC with considerable coolant mass flux, due to the lower operating temperature of Inconel.

**Keywords:** *aerothermodynamics, thermal protection system, transpiration cooling*

## Nomenclature

*Latin*

$B*$ – Boundary layer blowoff parameter
$B_h$ – Blowing parameter
$C_p$ – Specific heat capacity [J/kgK]
$F$ – Blowing ratio
$h$ – Enthalpy [J/kg]
$h_v$ – Volumetric heat transfer coefficient [W/m$^3$K]
$k$ – Thermal conductivity [W/mK]
$k_b$ – Shape factor
$k_D$ – Darcy coefficient [m$^2$]
$k_F$ – Forchheimer coefficient [m]
$L/D$ – Lift to drag ratio
$Le$ – Lewis number
$\dot{m}$ – Mass flux [kg/m$^2$s]
$N_{\text{inf}}$ – Coolant atomicity factor
$n$ – Number of Bezier points
$P$ – Pressure [Pa]
$Pr$ – Prandtl number
$Q$ – Heat load [J/m$^2$]
$\dot{q}$ – Heat flux [W/m$^2$]
$R_{LE}$ – Leading edge radius [m]
$St$ – Stanton number
$s$ – Surface coordinate [m]
$s$=0 – Stagnation point
$T$ – Temperature [K]
$u$ – Porous velocity
**u** – Porous velocity vector [m/s]
$v$ – External flow velocity [m/s]
$W$ – Molecular weight [g/mol]

*Greek*

$\alpha_w$ – Wedge angle
$\epsilon$ – Emissivity
$\theta$ – Subtended angle [rad]
$\mu$ – Viscosity [Pas]
$\rho$ – Density [kg/m$^3$]
$\sigma$ – Stefan-Boltzmann constant [W/m$^2$K$^4$]
$\phi$ – Porosity

*Subscripts*

amb – Ambient
aw – Adiabatic wall
conv – Convective
$d$ – Dissociation property
$e$ – Boundary layer edge
ext – On external surface

[1] *Oxford Thermofluids Institute, University of Oxford, Oxford, United Kingdom, OX2 0ES. Corresponding author email address: raghul.ravichandran@eng.ox.ac.uk*

$f$ – Fluid in porous medium
$hw$ – Hot wall
inj – Coolant property at injector surface
int – On internal surface
$n$ – Normal to boundary
operate – Operational limit
pl – Plenum
$s1$ – Porous solid matrix
$s2$ – Downstream solid
$w$ – Wall condition
0 – Uncooled
$\infty$ – Freestream

## 1. Introduction

One of the key challenges of hypersonic vehicle design is mitigation of the intense heat fluxes on a vehicle surface throughout its trajectory, to ensure that the heat load on the vehicle does not lead to temperatures contributing toward material failure. The thermal protection system (TPS) of any such vehicle must be designed to alleviate these high heat fluxes. In the case of extended duration missions, the TPS at must also manage the heat load. Another area of interest in hypersonic vehicle design is in improvement of vehicle performance parameters such as range and manoeuvrability, of which the lift-to-drag ratio ($L/D$) [1] is a key component. Reduction in leading edge bluntness has been identified as a means to improve $L/D$ across multiple mission profiles including re-entry [2], glide [3], and steady cruise [4].

Since the leading edge radius, $R_{LE}$, is inversely proportional to the square of the heat flux [5], there is a trade-off between improved aerodynamic performance via sharper leading edges, and TPS selection. A TPS applied to sharp leading edges must also ensure external shape stability, which would ensure aerodynamic performance is not affected over the trajectory, and allows for reusability of the vehicle.

Examples of historical missions' maximum cold wall stagnation point heat flux and heat loads are shown in Figure 1. Points have been added for a generic glide trajectory [6] with different $R_{LE}$. It is seen that high heat flux, short duration missions are associated with ablative systems, where TPS mass fraction increase linearly with heat load [7], up to 50% for the Galileo probe. The increasing mass penalty of an ablative TPS under high heat loads, combined with the limited space of a sharp leading edge, and the necessity for shape stability mean that an ablative TPS may not be suitable for high heat load trajectories.

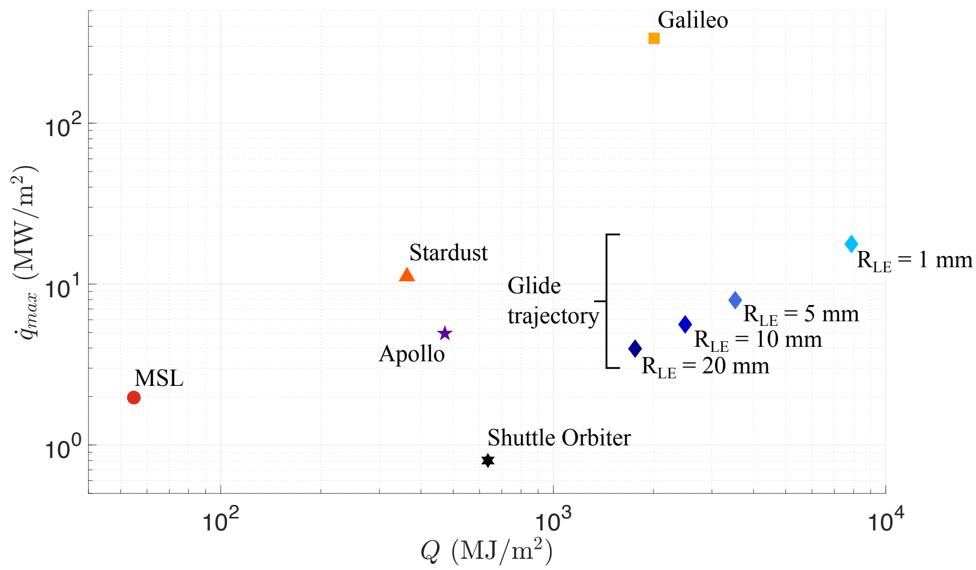


**Fig 1.** Stagnation point cold wall heat flux and heat loads of historical missions [5, 8, 9, 10] versus that of a generic glide trajectory [6] with different $R_{LE}$ values.

Low heat flux, longer duration missions missions are associated with passive systems. One candidate material for a passive hot structure TPS is C/C-SiC [2], which has high heat capacity and operating temperature to store and reject heat through re-radiation into the atmosphere. Such strategies work in steady-state missions where the incoming heat flux can be balanced by the re-radiation of the hot structure. Active oxidation of the SiC matrix is difficult to control and may occur under certain pressure and temperature combinations, which may lead to leading edge degradation and failure [11].This TPS strategy will be modelled and compared to transpiration-cooled leading edges in this paper.

For applications where passive systems do not provide sufficient protection, and ablative systems cannot provide shape stability over the whole mission, active systems could be employed in a targeted manner to mitigate the intense heat fluxes. Active TPS strategies are associated with volume, mass, and complexity penalties, and so a new trade-off is created: that between the thermal balance, the aerodynamics of the vehicle, and the penalties of an active TPS.

Transpiration cooling is a promising active TPS candidate where coolant is injected through a permeable wall into the hypersonic boundary layer, shown in Figure 2. Thermal protection is provided by three simultaneous mechanisms:

1. Internal convective heat transfer between the hot porous matrix and the coolant gas passing through
2. Film cooling, where the coolant gas is swept downstream, forming a coolant layer that reduces thermal gradients and therefore heat flux
3. Chemical protection barrier formed by the coolant film, reducing catalytic wall heating effects and delaying material oxidation.

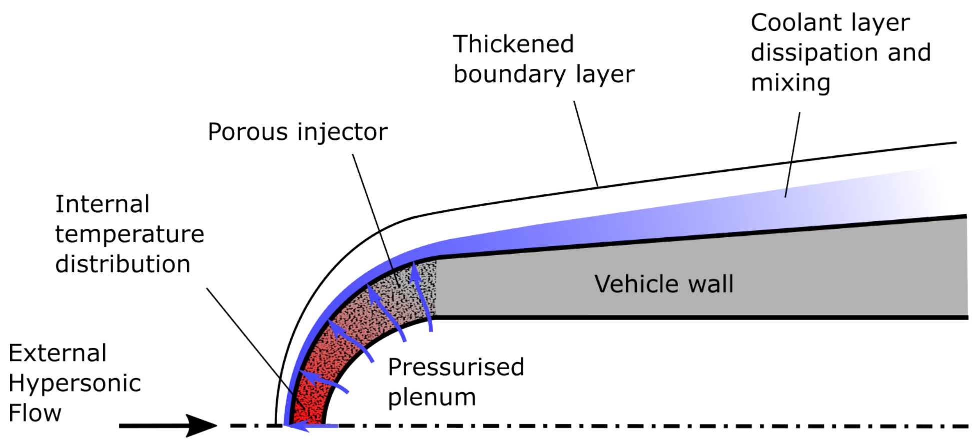


**Fig 2.** A sketch of a transpiration-cooled leading edge.

Transpiration cooling has been studied as a TPS candidate since the 1950s. A variety of geometries have been studied to better characterise heat flux reduction due to transpiration cooling, including axisymmetric stagnation point injectors [12, 13, 14], flat plates [15, 16], blunt bodies [17], and downstream frustum injectors [18].
For a stagnation point injector, the blowing parameter, $B_h$, is a mass injection parameter that is frequently used to predict heat flux reduction [13, 19, 20, 21]. $B_h$ is defined using the uncooled Stanton number, $St_0$ and blowing ratio, $F$, as defined in Equations 1-3.

$$B_h = \frac{F}{St_0(s)} \tag{1}$$

$$F(s) = \frac{\dot{m}_{\text{inj}}(s)}{\dot{m}_\infty} = \frac{\rho_{\text{inj}} u_{\text{inj}}}{\rho_\infty u_\infty} \tag{2}$$

$$St_0(s) = \frac{\dot{q}_0(s)}{\rho_\infty u_\infty (h_{aw} - h_w)} \tag{3}$$

A semi-analytical correlation [13] links $B_h$ to stagnation point heat flux reduction, and has been experimentally [20] and numerically [21] verified. This correlation is shown below in Equation 4. Here, $B*$ is known as the 'boundary layer blow-off parameter', whereby if $B_h > B*$, the boundary layer is significantly disturbed, promoting transition and increasing heat flux. Work has shown that for blunted leading edges, mass injection below the $B*$ limit does not affect the surface pressure field [22], whereas excessive blowing far beyond $B*$ increases downstream pressure and negates the aerodynamic of sharp leading edges [17]. This effect forms an important constraint for a transpiration-cooled system, however it has not been fully quantified in literature for blunt geometries.

$$\Psi = \frac{\dot{q}(0)}{\dot{q}_0(0)} = \sqrt{\pi\Lambda}\frac{\text{exp}\{-\Lambda {B_h}^2\}}{1+\text{erf}\{\Lambda\}^{0.5}B_h} \tag{4a}$$

$$\Lambda = \frac{1}{\pi}\frac{\Delta}{\Delta^{uc}}\lambda^{B_h/B*} \tag{4b}$$

$$B* = 1.82\frac{\sqrt{\pi\epsilon(W_f/W_\infty}}{k_b(\chi_w')^*} \tag{4c}$$

$$(\chi_w')^* = \frac{1.187\sqrt{(8\epsilon(1-\epsilon)}}{(1+\sqrt{8/3\epsilon)}-\epsilon)(1+0.225\sqrt{\epsilon})} \tag{4d}$$

$$\lambda = \sqrt{\frac{W_\infty}{W_{\text{inj}}}}N_{\text{inj}} \tag{4e}$$

$$\frac{\Delta}{\Delta_0} = 1 + k_b\sqrt{\frac{1}{\epsilon}\frac{W_\infty}{W_{\text{inj}}}}F \tag{4f}$$

$$\epsilon = \frac{\rho_\infty}{\rho_1} \tag{4g}$$

$$\tag{4h}$$

In [22], it was shown numerically that the stagnation point correlation in Equation 4 could be extended to 2D space for a leading edge injector on a planar blunted wedge, and that film cooling effects over the curved injector are negligible, up to a leading edge radius, $R_{LE}$, of 25 mm. Downstream of the injector, film cooling is the primary heat flux reduction mechanism. Along external surface coordinate, $s$, local heat flux reduction on a blunted leading edge injector may be described using Equation 5. Here, the same flowfield properties in Equation 4 are evaluated locally round the injector, rather than on the stagnation line.

$$\Psi(s) = \frac{\dot{q}(s)}{\dot{q}_0(s)} \tag{5}$$

Previous numerical work has been carried out to assess the performance transpiration-cooled TPS strategies. In [23], a heat balance of a transpiration-cooled flat plate subject to an external flow boundary layer is carried out. A finite-difference code, *HEATS*, is developed to calculate the mass flux requirements of a constant-thickness, transpiration-cooled flat plate in flight, mainly in the context of the flight experiment, SHEFEX [24]. In [25], the heat balance was recast by using thermal impulse and step responses of solid material to calculate temperature distributions to improve calculation time. This impulse response code, *PIRATE*, considered internal conduction and porous flow in 1D segments, under the assumption that wall thickness is much less than leading edge radius. Semi-empirical correlations for aerodynamic heat flux and film effectiveness were used, taken from a mixture of flat plate and blunt body experimental studies. In [26], *PIRATE* was employed to assess the operating regime and mass flux distribution requirements of a transpiration-cooled conical nosetip, blunted with radius $R_{LE}$ = 0.5 m. Here, the operational limits were mainly based on flat-plate blowing limits. Mass flux requirements and spatial distributions were calculated for steady cruise and transient trajectories. Internal structure or means of distributing mass flux was not considered. For steady cruise, transpiration cooling was shown to be beneficial for velocities between 5.5-8 km/s and altitudes between 30-55 km.

This paper aims to update the methodology to design and calculate an operating envelope for a transpiration-cooled leading edge. Since sharp leading edges are being considered, a thin-wall assumption cannot be used, and so the heat transfer and porous flow processes must now be considered in 2D. Updated cooling correlations [13, 15, 22] can be used on, and downstream of, the leading edge injector. Finally, the internal structure of the leading edge is considered and designed to understand how the required mass flux distributions may be achieved.

## 2. Model Setup

The numerical tool was run using the finite element solver *COMSOL Multiphysics*. All calculations are run in steady state. A block diagram of the tool is shown in Figure 4. The inputs are: flight condition (velocity-altitude pair), material, leading edge radius, and coolant gas. The tool calculates the incoming, uncooled convective heat flux distribution and surface pressure. After initialisation, the coupled solver is employed to solve for heat exchange between the solid and coolant, and the porous flow of the coolant through the injector. The internal geometry is controlled by an optimisation loop to distribute the mass flux and bring the leading edge to within operating limits using the minimum coolant possible. Details on the optimisation loop for the internal geometry are given in Section 2.6.

When assessing how transpiration cooling performs, the limits are dictated by the performance of a passive TPS under the same conditions, and the blowing parameter requirements. If a passive TPS is shown to survive under the same heat flight conditions, the extra complexity of an active TPS is not needed. As discussed earlier, if the required $B_h >> B*$, the conditions are considered to be too severe for transpiration cooling. It is only when $B_h < B*$ and the passive TPS does not survive that transpiration is considered to be beneficial.

### 2.1. External Surface Geometry

In-line with previous work [22], the geometry was considered to be a 2D cylindrically blunted wedge with leading edge radius $R_{LE}$ and half-angle $\theta_w = 5°$, shown in Figure 3. The base length was scaled with the radius such that $L_{BASE} = 10R_{LE}$. The porous injector exists only around the curvature of the leading edge. On the external surfaces, heat flux and pressure distributions were calculated, shown below.

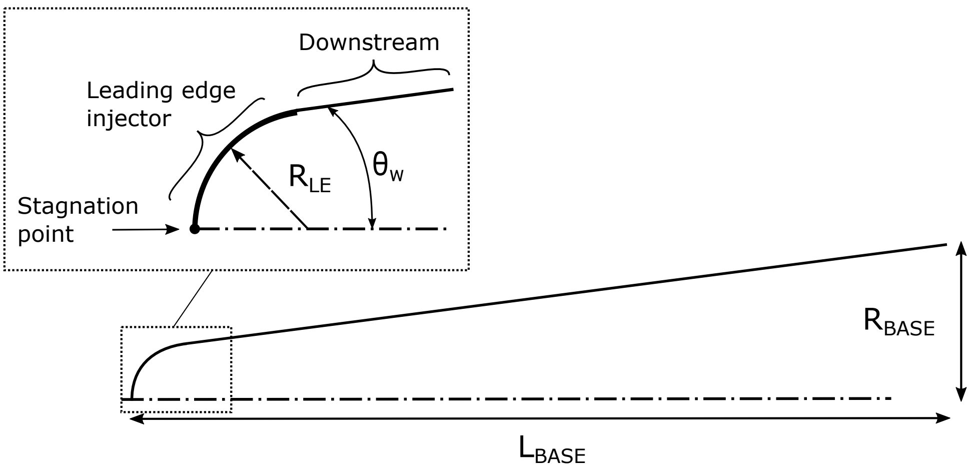


**Fig 3.** A sketch of the 2D external geometry for heat flux calculations.

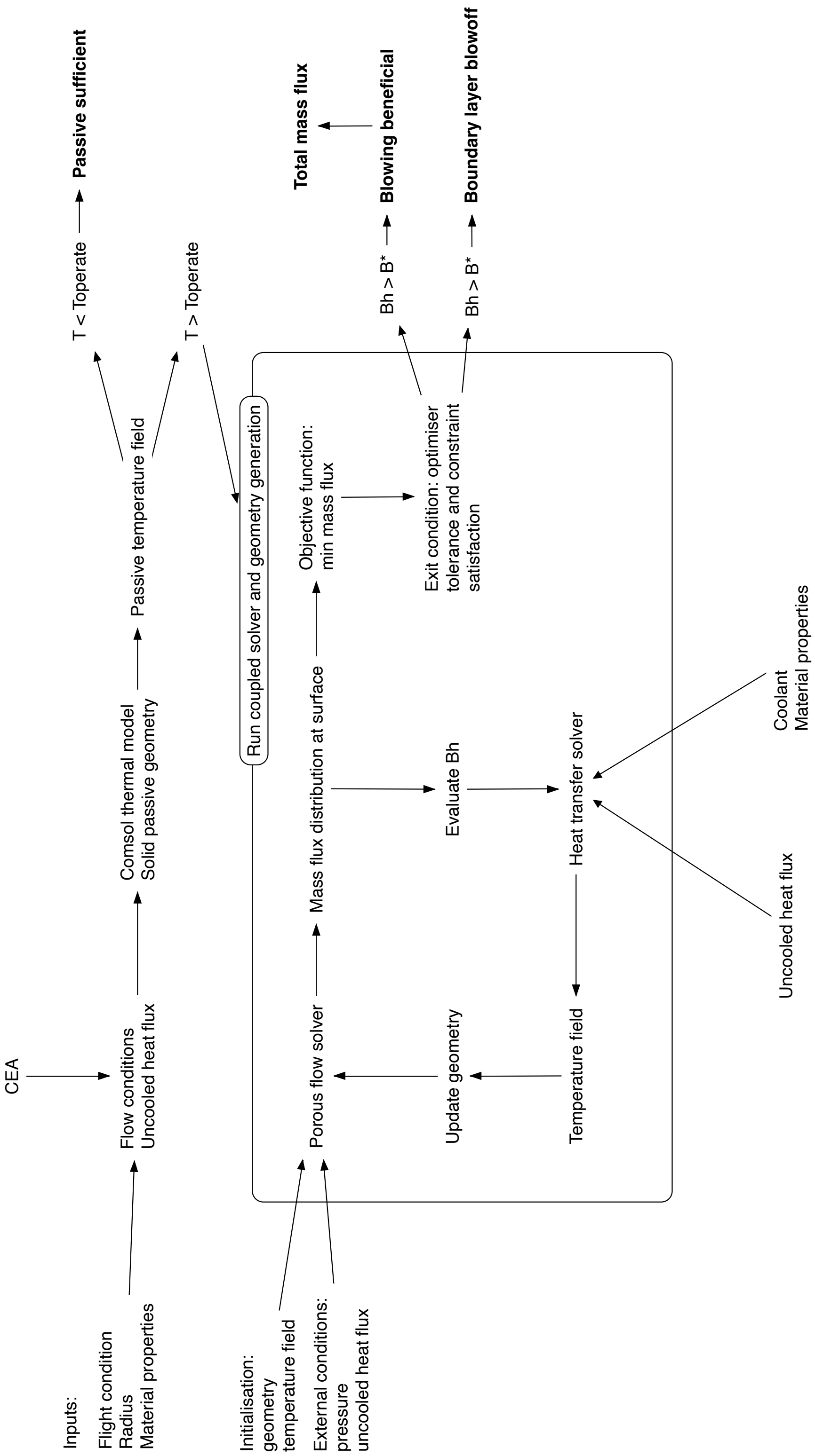


**Fig 4.** Block diagram of leading edge coupled solver.

### 2.2. Boundary Conditions and Governing Equations

The domain consists of a porous injector with solid and fluid in thermal non-equilibrium, joined to an impermeable downstream wedge. Inside the injector, there is a two-temperature problem, where the energy equations must be solved for the fluid, $T_f$, and porous solid $T_{s1}$ simultaneously. The domains and boundary conditions of the numerical tool for are shown below in Figure 5. Descriptions and governing equations for each domain and boundary condition are given in Tables 1 and 2.

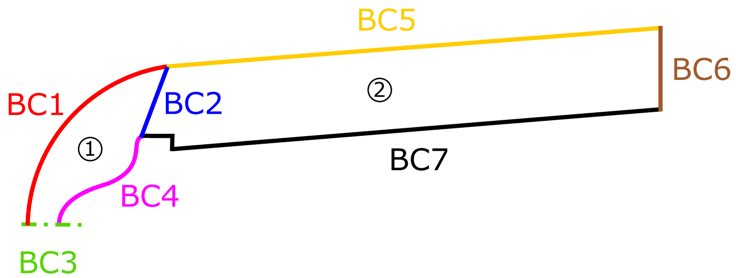


**Fig 5.** Heat transfer boundaries

**Table 1.** Governing equations for coupled solver.

| Domain | Description | | Equations |
|---|---|---|---|
| ① | Heat transfer | Solid: | $k_s(1-\phi)\nabla^2 T_{s1} + h_v(T_{s1} - T_v) = 0$ |
| | | Fluid: | $\rho_f C_{p,f} \frac{\mathbf{u}}{\phi} \nabla T_f + h_v(T_f - T_{s1}) = 0$ |
| | Porous flow | | $\nabla P = -\frac{\mu}{k_D}\mathbf{u} - \frac{\rho}{k_F}\lvert\mathbf{u}\rvert\mathbf{u}$ |
| ② | Heat transfer | | $k_s(1-\phi)\nabla^2 T_{s2}$ |

### 2.3. External Heat Flux and Pressure

For a given flight condition, freestream and post-shock stagnation line gas properties were estimated using the U.S. 1976 Standard atmosphere and NASA's Chemical Equilibrium with Applications (CEA) program [27, 28]. Post-shock conditions were assumed to be in thermochemical equilibrium, and without wall catalycity. Uncooled heat flux at the stagnation point was calculated using the Fay-Riddell [29] correlation, modified for a 2D planar geometry [30], shown in Equation 6. Here, $h_w$ is the hot-structure wall enthalpy.

$$\dot{q}_{FR}(0) = \frac{0.438}{Pr_w^{0.6}}(\rho_e \mu_e)^{0.42}(\rho_w \mu_w)^{0.08}(h_{0,e} - h_w)\left(1 + (Le^{0.52} - 1)\frac{h_d}{h_{0,e}}\right)\left(\frac{dv_e}{dx}\right)^{0.5} \tag{6}$$

Here, velocity gradient is estimated from Netwonian theory in Equation 7.

$$\frac{dv_e}{dx} = \frac{1}{R}\sqrt{\frac{2(P_e - P_\infty)}{\rho_e}} \tag{7}$$

The coolant film that forms on injector acts as an intermediate layer between the hot wall and the hot post-shock gas. The film correction factor used for a hot wall with cooler gas used in [25] is given by Equation 8, where $h_{r,inj}$ and $h_r$ are the recovery enthalpies of the local coolant outflow gas, and the

**Table 2.** Boundary conditions for coupled solver.

| Physics | Boundary | Description | Equation |
|---|---|---|---|
| Porous flow | BC1 | Outlet: pressure distribution | $P = P_{\text{ext}}(s)$ |
| | BC2 | No flow | $\rho u_n = 0$ |
| | BC3 | Symmetry | $\rho u_n = 0$ |
| | BC4 | Inlet: pressure | $P = P_{\text{pl}}$ |
| Heat transfer | BC1 | Solid: heat flux + cooling + re-radiation | $\dot{q}_{\text{in},s1} = \psi \dot{q}(s)_{\text{conv, hw},s1} - \epsilon_{\text{ext}}\sigma\left(T_{\text{ext},s1} - T_{\text{amb,ext}}\right)^4$ |
| | | Fluid: Adiabatic outlet | $\dot{q}_f = 0$ |
| | BC2 | Solid: Thermal continuity | $T_{s1} = T_{s2}$ |
| | | Fluid: Adiabatic | $\dot{q}_f = 0$ |
| | BC3 | Solid: Symmetry | $\dot{q}_{s1} = 0$ |
| | | Fluid: Symmetry | $\dot{q}_f = 0$ |
| | BC4 | Solid: Backside re-radiation | $\dot{q}_{\text{out},s1} = \epsilon_{\text{int}}\sigma\left(T_{\text{int},s1} - T_{\text{amb}}\right)^4$ |
| | | Fluid: Temperature inlet | $\dot{q}_f = 0;\ T_f = T_{\text{int}}$ |
| | BC5 | Downstream heat flux + re-radiation | $\dot{q}_{\text{in},s2} = \dot{q}(s)_{\text{conv, hw},s2} - \epsilon_{\text{ext}}\sigma\left(T_{\text{ext},s2} - T_{\text{amb,int}}\right)^4$ |
| | BC6 | Adiabatic | $\dot{q}_f = 0$ |
| | BC7 | Backside re-radiation | $\dot{q}_{\text{out},s2} = \epsilon_{\text{int}}\sigma\left(T_{\text{int},s2} - T_{\text{amb,int}}\right)^4$ |

post-shock gas, respectively. The coolant temperature at the surface must therefore be evaluated on iterations of the solver to re-evaluate the incoming heat flux.

$$\dot{q}(0) = \dot{q}_{FR}(0)\ \frac{h_{r,inj} - h_w}{h_r - h_w} \tag{8}$$

Lees' [31] correlation in Equation 9 was employed for the heat flux distribution around a blunted body.

$$\dot{q}(s) = \begin{cases} \dot{q}(0)\cdot D^{-0.5}\left[2\theta\sin(\theta)[(1-K_\infty)\cos^2(\theta) + K_\infty\right] & \text{for } \theta \leq \frac{\pi}{2} - \alpha_w \\ \dot{q}(0)\cdot A\dfrac{(s'/R_{LE})}{\sqrt{B + (s'/R_{LE})^3}} & \text{for } \theta > \frac{\pi}{2} - \alpha_w \end{cases} \tag{??}$$

where

$$D = (1-K_\infty)\left(\theta^2 - \frac{\theta\sin(4\theta)}{2} + \frac{1-\cos(4\theta)}{8}\right) + 4K_\infty\left(\theta^2 - \theta\sin(2\theta) + \frac{1-\cos(2\theta)}{2}\right) \tag{9a}$$

$$s' = R_{LE}\left[\cot(\alpha_w) + \frac{s}{R_{LE}} - \left(\frac{\pi}{2} - \alpha_w\right)\right] \tag{9b}$$

$$A = \frac{\sqrt{3}}{2}\sqrt{(1-K_\infty)\sin^2(\alpha_w) + K_\infty}\sqrt{\frac{\pi}{2} - \alpha} \tag{9c}$$

$$B = \frac{3}{16}\left[\sin^2(\alpha_w)(1-K_\infty)\sin^2(\alpha) + K_\infty\right]^{-1}\frac{D\Big|_{\theta=\pi/2-\alpha_w}}{\pi/2 - \alpha_w} - \cot^3(\alpha) \tag{9d}$$

$$K_\infty = \frac{1}{\gamma_\infty M_\infty^2} \tag{9e}$$

In order to operate at steady-state, the incoming convective heat flux is balanced by several mechanisms: incoming heat flux is reduced by a smaller driving enthalpy difference due to the hot structure; active heat flux rejection by re-radiation; heat flux reduction due to blowing; temperature reduction due to fluid-solid heat exchange; and lateral conduction from the solid at the stagnation to the downstream, cooler solid. This balance is shown for BC1 when solving for heat transfer. External pressure, also enforced on BC1, was estimated using a Modified Newtonian pressure distribution, where post-shock pressure was also calculated using CEA.

### 2.4. Model Coupling

The COMSOL solver directly couples **u** and $T_f$. The porous flow solver calculates the velocity field **u**, which affects the rate of fluid-solid heat exchange and therefore fluid temperature $T_f$. Inversely, the fluid temperature field $T_f$ is calculated by the heat transfer solver and affects the fluid viscosity, $\mu$ through Sutherland's law: $\mu_f = \mu_f(T_f)$. An increase in $\mu_f$ decreases **u**, known as viscous blockage, which requires a larger driving pressure gradient to maintain the same coolant mass flux.

Both porous flow and heat transfer solutions are iterated until the flowfield variable residuals fall below a certain threshold. There are also less direct couplings in the steady-state calculation. In this study, the coolant mass flux is controlled by a single plenum and a variable thickness porous material. High temperature regions therefore require thinner material to drive more coolant through. This heat flux reduction must be traded-off with lateral conduction effects that also reduce the temperature around the stagnation point. Wall temperature, $T_w$, affects re-radiative heat flux out, hot-wall convective heat flux, and $B_h$: all of which must be re-evaluated with wall temperature on each iteration.

### 2.5. Assumptions

The governing equations and boundary conditions operate under a series of assumptions, listed below.

***Flow Conditions***

- The flow is thermochemical equilibrium.
- Wall catalysis and oxidation is not considered, nor mitigated by transpiration cooling.

***Porous Flow***

- Mass injection does not affect the external pressure field, supported in [22].
- The porous matrix contains fully open porosity, and has uniform isotropic permeability.

***Heat Transfer***

- Porous matrix thermal properties ($\rho_s,\ C_{p,s},\ k_s$) are volume-averaged with respect to that of the fully the fully dense materials.
- Fully saturated porous medium
- Primary source of fluid heat transfer is internal convection within the porous matrix. There is negligible heat transfer via fluid conduction, and from the solid wall to the fluid in BC2.
- Heat flux distribution assumes a zero angle of attack.
- Internal temperature, $T_{\text{int}}$, and fluid temperature at the porous inlet, $T_f$ are 300 K.

### 2.6. Internal Geometry and Optimisation Algorithm

The coolant mass flux must achieve two things: overcome the external surface pressure, and must be highest in the regions where the leading edge is hottest, which is made more difficult by incrasing viscous losses. Mass flux delivery In this study, the mass flux distribution is controlled by the thickness distribution of the porous matrix and the plenum pressure. Shown in Figure 6a, the external surface of the leading edge must remain the same, therefore the only method of changing the porous matrix thickness is by changing the geometry of the internal wall.

The internal geometry was constructed using Bezier curve, the coordinates of the control points of which were parameterised as shown in Figure 6b. The $n$ control points were distributed evenly in the $y$ direction across $y = 0$ to $y_{\text{pl}}$, and in the $x$ direction by a series of lengths, $L_i$, from an anchor coordinate, $x_{\text{anchor}} = R_{LE}$.

The optimisation problem was defined as a mass flux minimisation problem: finding the minimum

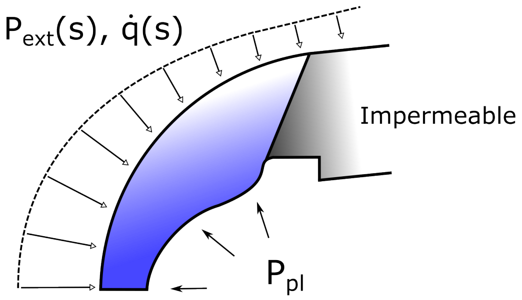


**(a)** Porous flow boundaries

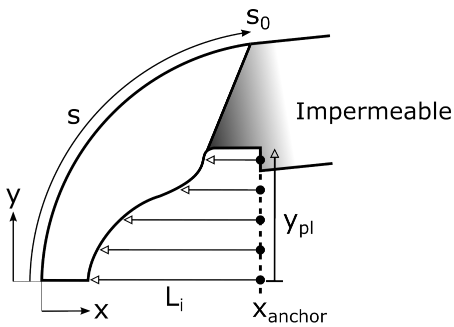


**(b)** Heat transfer boundaries

**Fig 6.** Internal boundaries for the porous flow.

total mass flux required to cool a leading edge to a target temperature via the heat flux reduction mechanisms described above. Described above, the 3 input parameters are: $L_i$, $P_{\text{pl}}$, and $y_{\text{pl}}$. The optimisation problem is therefore written as below:

$$
\begin{aligned}
\text{minimize} \quad & \dot{m}_{\text{tot}} = \int_0^{s_0} \dot{m}_{\text{inj}}\, ds & \\
\text{subject to} \quad & T_s(x, y) \le T_{\text{operate}} & \\
& y_{\text{pl}} \le y_{\text{surf}}\big|_{x = x_{\text{anchor}}} & \\
& y_{\text{pl}} \ge 0 & \\
& L_i \ge 0 & i = 1, \ldots, n \\
& L_i \le x_{\text{anchor}} - x_{\text{surf}}\big|_{y = y_i} & i = 1, \ldots, n \\
& L_1 = 0.3 R_{LE} & i = 1, \ldots, n \\
& L_i \le L_{i-1} & i = 1, \ldots, n
\end{aligned}
\tag{10}
$$

The first constraint is the primary means by which a target temperature is maintained. The combination of an operational temperature and a minimum mass flux objective function was sufficient to keep the temperature of the leading edge right at the operating temperature. The next four constraints provide upper and lower bounds for the $(x, y)$ coordinates of the Bezier curve, to prevent intersection with the external geometry. Finally, the last two constraints (which may override the others) speed up the search for the minimum objective function. In particular, specifying the length on the stagnation line, $L_1$, allows the solver to find $P_{\text{pl}}$ for the stagnation line problem and proceeding with the rest of the geometry after.

The optimisation algorithm used was *MATLAB*'s in-built hybrid particle swarm optimiser (PSO) with *fmincon*, where a PSO problem was run to find an initial solution for *fmincon*. Since the problem is highly non-linear, *fmincon* uses a finite difference sampling method to obtain local gradients. The PSO was run with *MATLAB*'s default options for the particle inertias and velocities [32]. The swarm span was set by the upper and lower bound constraints above.

## 3. Performance Study

### 3.1. Setup

A preliminary performance study was carried out to gain an insight into the operational envelope of a transpiration-cooled leading edge. For each flight condition, the external heat flux and pressure were calculated as described in Section 2.3. For a material with given operational temperature, the 2D heat transfer solution was run to calculate the uncooled temperature of the leading edge. If the uncooled temperature field exceeds the operating temperature, the coupled solver is employed within the optimisation loop to calculate a internal geometry and coolant pressure required to bring the leading edge to within material limits. The study therefore examines survivability of an on-condition geometry at steady flight conditions. For a range of altitudes of 10-60 km and velocities of 1-6.5 km/s, two leading edge materials (Inconel 625 and tungsten) were tested for 3 different radii (1, 3, 5 mm) with nitrogen and helium gas coolant. The material-specific properties are shown in Table 3. Permeability and volumetric heat transfer coefficient are assumed to consistent across the porous materials, and emissivity is assumed to be the same for both passive and actively-cooled material. Coolant gas properties are shown in Table 5. $h_v$ is the internal volumetric heat transfer coefficient, where higher $h_v$ corresponds to more efficient equalisation of temperature between solid and coolant within the porous flow. $k_D$ and $k_F$ are the Darcy and Forchheimer coefficients respectively, dictating porous material permeability. The values of $h_v$, $k_D$ and $k_F$ were selected from experimental results in [33, 34] for sintered particles of high performance metals, similar to the materials selected in this study [35].

**Table 3.** Solid material properties evaluated at 300 K [24, 36, 37].

| Material | $T_{\text{operate}}$ (K) | $k_s$ (W/mK) | $C_{p,s}$ (J/kgK) | $\rho$ (kg/m$^3$) |
|---|---|---|---|---|
| Inconel 625 | 1600 | 9.75 | 411 | 8250 |
| Tungsten | 2000 | 175 | 132 | 19300 |
| C/C-SiC | 1950 | 17 | 1350 | 1900 |

**Table 4.** Assumed porous properties and emissivity for re-radiation.

| $\phi$ | $k_D$ (m$^2$) | $k_F$ (m) | $h_v$ (W/m$^3$K) | $\epsilon$ |
|---|---|---|---|---|
| 0.4 | 2.162E-12 | 1.023E-6 | 5E5 | 0.8 |

**Table 5.** Coolant properies evaluated at 300 K [36].

| Coolant | $k_s$ (W/mK) | $C_{p,f}$ (J/kgK) | $\rho$ (kg/m$^3$) | $\mu$ (Pas) | $W_f$ (g/mol) |
|---|---|---|---|---|---|
| Nitrogen | 0.026 | 1040 | 1.15 | 1.8E-5 | 28 |
| Helium | 0.15 | 5200 | 0.163 | 2.1E-5 | 4 |

If a passive system is feasible for a given design condition, it would be a more attractive strategy due to the smaller mass, volume and complexity penalties. A re-radiating C/C-SiC leading edge was run to find the steady state temperature for each flight condition, using the boundary conditions shown in Figure 7. The same geometries were used as the active cooling cases to form a direct comparison. Conditions where the passive system fails but the actively-cooled system survives were considered to be regions where transpiration cooling may be considered beneficial.

 

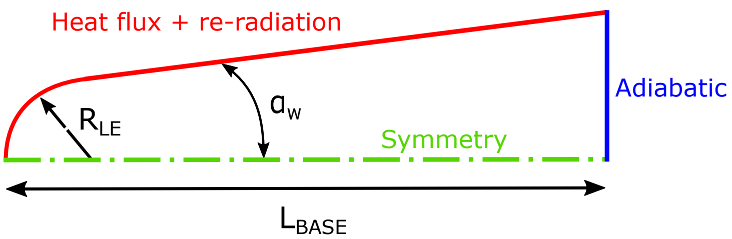


**Fig 7.** Passive case boundary conditions.

### 3.2. Constraints

The two main limits for the regimes are:

1. Lower limit: regions where no transpiration cooling is required. These are conditions not only where a porous leading edge survives with mass flux set to zero, but also where a benchmark passive TPS would also function. Results from the passive TPS are given in Section 4.1.

2. Upper limit: regions where required cooling is excessive. Discussed in Section 1, if $B_h$ exceeds a critical parameter $B*$, boundary layer blow-off may occur, which may increase downstream pressure drag and heat flux, and should be avoided. While a formal analysis of this effect for blunted wedges has not been carried out before, $B_h = B*$ may be used as a guide for being close to the upper operating limits of transpiration cooling.

## 4. Results

### 4.1. Passive TPS

A temperature field for the C/C-SiC leading edge at a given flight condition is shown in Figure 8. While re-radiation and lateral conduction reduce the temperature at the stagnation point, the stagnation point heat flux under these conditions (3.6 MW/m$^2$) is too high to dissipate passively, and so the material operating temperature is exceeded. This condition would therefore be considered for transpiration cooling. A map of passive TPS wall temperature against flight conditions is shown in Figure 9.

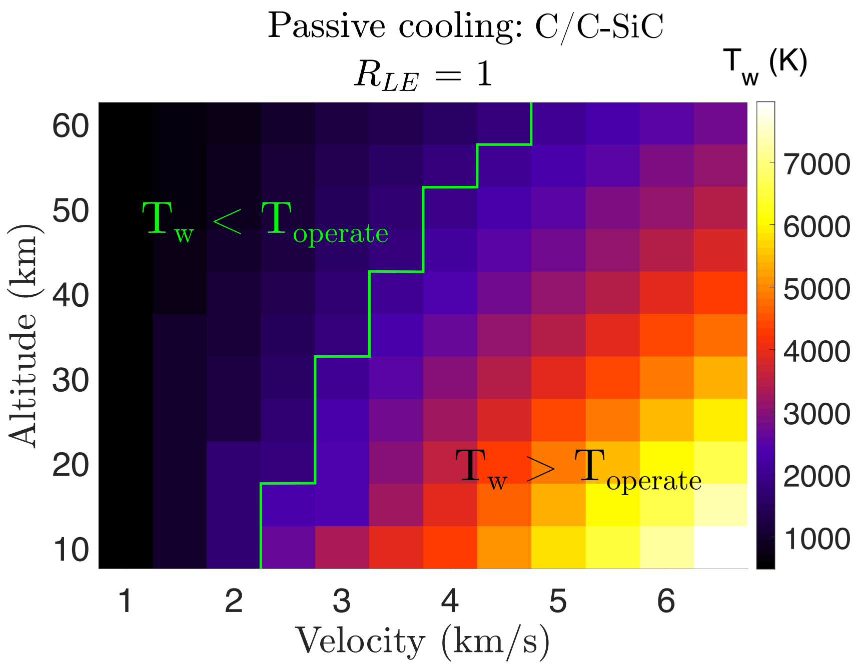


**Fig 9.** Stagnation point wall temperature for different flight conditions of a 1 mm radius C/C-SiC leading edge.

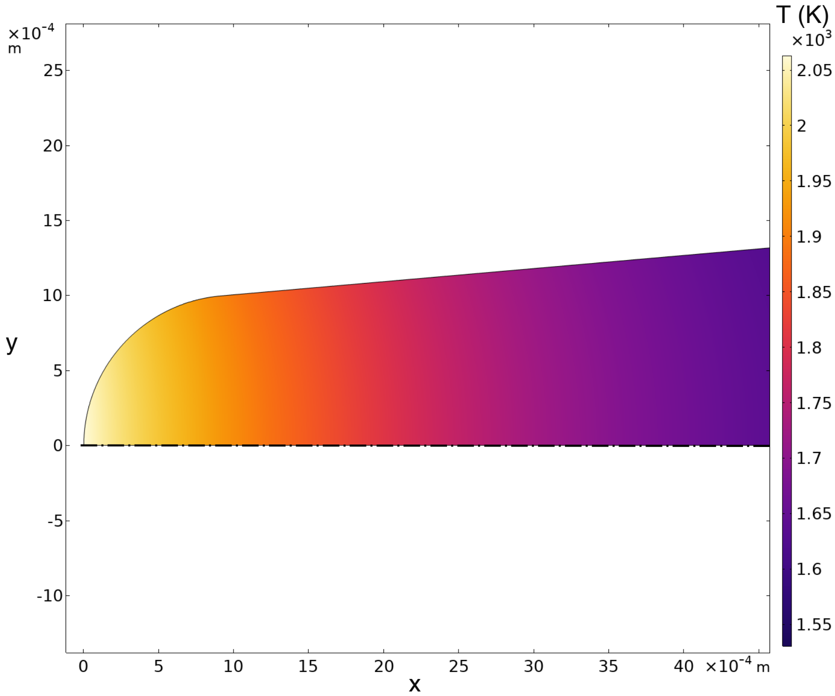


**Fig 8.** Temperature field of a 1 mm radius C/C-SiC leading edge for $v_\infty$ = 3.5 km/s and altitude = 40 km. The domain is truncated to $x$ = $4R_{LE}$.

### 4.2. Transpiration Cooling

This study investigates how to actively cool a leading edge at a specified temperature for given flight conditions, by contouring the internal geometry to minimise the amount of coolant mass flux. A plot of steady state internal temperature of the solid and fluid is shown in Figure 10. The shape of the converged internal structure of the injector is also shown. The optimiser strongly targets stagnation point cooling by making the wall very thin, and quickly increases wall thickness around the leading edge. Moving around the leading edge, the external pressure and heat flux drop rapidly, and so the thickness distribution increases quickly to reduce coolant mass flux.

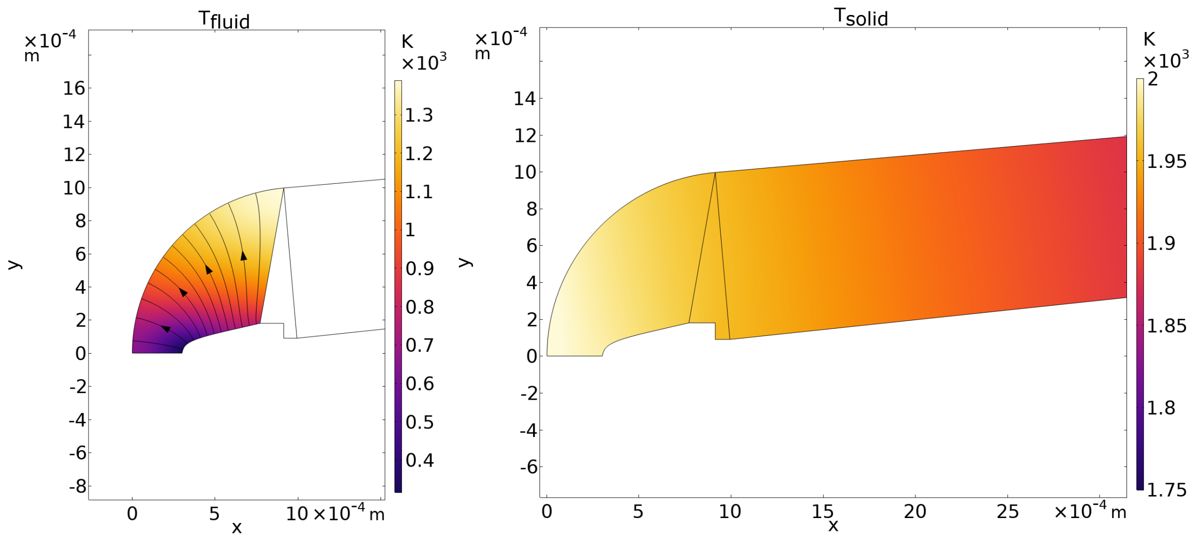


**Fig 10.** Temperature fields of solid and fluid for a 1 mm tungsten leading edge with nitrogen coolant at $v_\infty$ = 3.5 km/s, altitude = 30 km. $P_{pl}$ = 2.42 bar. The solid domain is truncated up to $x = 3R_{LE}$.

The plot of $T_s$ shows that high conductivity of tungsten is beneficial by diffusing the high temperature away from the stagnation point. The plot of $T_f$ suggests internal heat transfer from solid to fluid occurs most in regions with a low internal coolant velocity and a thicker porous medium to flow through. While the fluid temperature at the stagnation point outlet does increase by 300 K, the very thin porous solid at the stagnation point will not be effective in cooling hottest region via fluid-solid heat exchange, unless $h_v$ were to spatially varied along the leading edge. While an increase in $h_v$ could more effectively internally cool the leading edge, hotter gas at the injector exit decreases the heat flux reduction by injection into the external flow. Further study could investigate the trade-off between these two cooling mechanisms by varying $h_v$.

Key transpiration cooling parameters are plotted along the leading edge surface in Figure 11. The surface temperature is successfully kept at and below the operating temperature of the material. As expected from the internal geometry, mass flux is concentrated right at the stagnation point and sharply falls away. In this case, the required $B_h$ does not exceed the condition's $B*$, and so is a viable case for transpiration cooling.

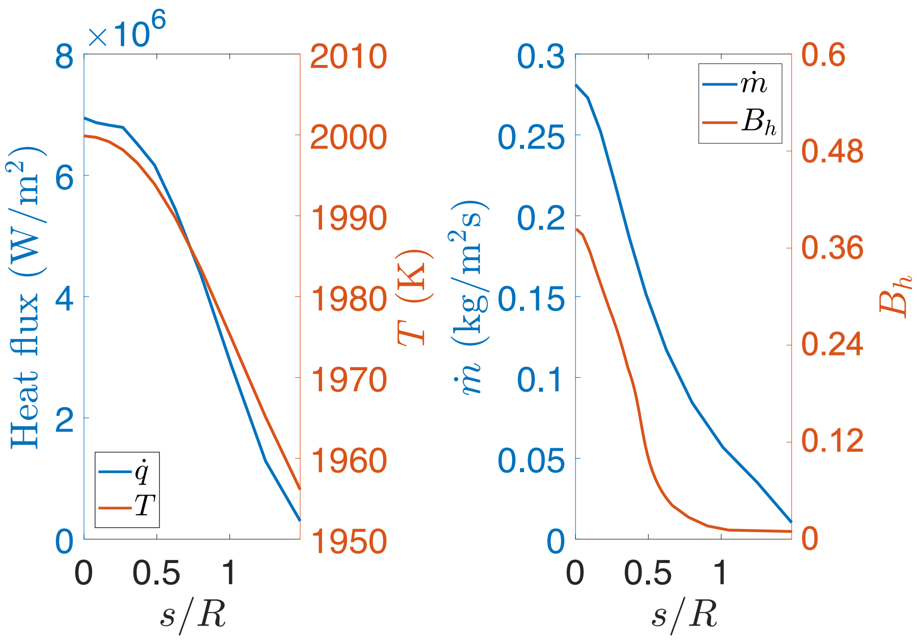


**Fig 11.** Surface profiles of $T_s$, $\dot{q}$, $B_h$ and $\dot{m}_{\mathrm{inj}}$, for a 5 mm tungsten leading edge with nitrogen coolant at $v_\infty$ = 3.5 km/s, altitude = 30 km. $P_{pl}$ = 2.42 bar

These solutions are generated for a range of flight conditions and compared to the passive results to form a operational envelope as shown in Figure 12, which shows a colourmap plot of maximum $B_h$ along the leading edge. These results may be plotted as contours of $B_h$ to compare the effect of different geometries, materials and coolants.

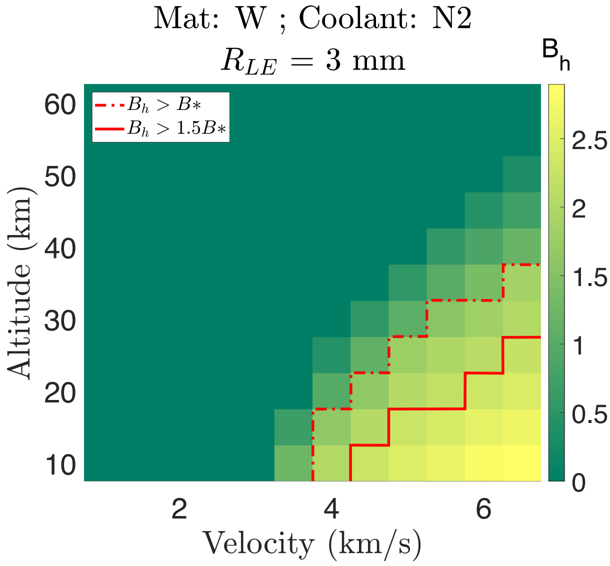


**Fig 12.** Maximum $B_h$ for each flight condition for a 3 mm radius tungsten leading edge using nitrogen coolant.

### *Effect of material*

In Figure 13, the very high operating temperature and conductivity of tungsten means that even without blowing, the tungsten is able to survive at conditions past that of the C/C-SiC leading edge. This may be because the protection of the C/C-SiC system is via thermal storage and hot structure re-radiation, which is feasible for transient trajectories on the order of several minutes, or lower magnitude heat fluxes in steady state. In Figure 13, Inconel must operate at lower velocities to tungsten due to its lower operating temperature. The band where transpiration cooling is required now begins to overlap with the passive TPS, and so the conditions where an actively-cooled system is beneficial is narrowed.

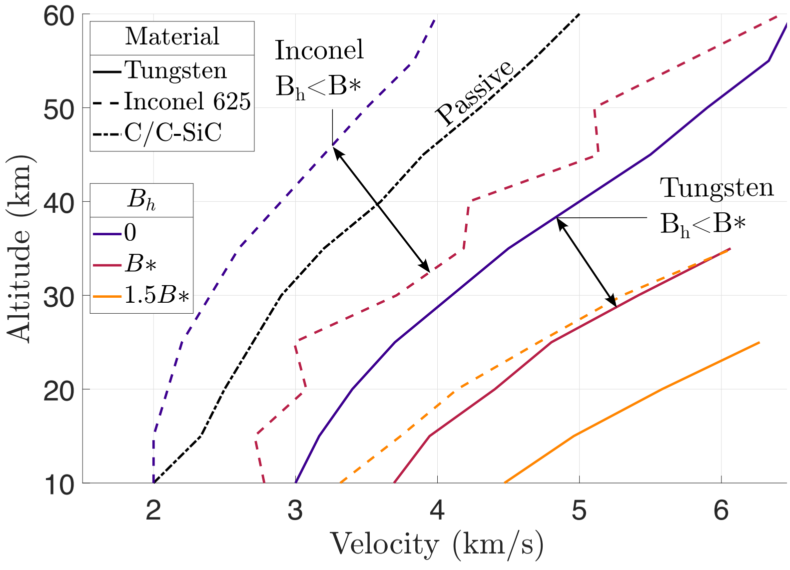


**Fig 13.** Effect of varying material. $R_{LE}$ = 3 mm, coolant: N2.

### Effect of Coolant

Helium is a more effective coolant at the same mass flux than nitrogen. It is selected as a coolant candidate in other feasibility and experiments [26, 38] due to its high heat capacity. However, this advantage is largely negated by the low internal convective heat transfer (Figure 10). In addition, Helium encounters a significant volume penalty due to its low density and storage options; and is more susceptible to boundary layer blowoff at a given mass flux due to its low molecular weight (Equation 4c). The trade-off between the blowoff behaviour and the cooling effectiveness is shown in Figure 14. While helium requires a lower $B_h$ to reach the same temperature as nitrogen, helium cannot cool to the same conditions as nitrogen without $B_h$ exceeding $B*$.

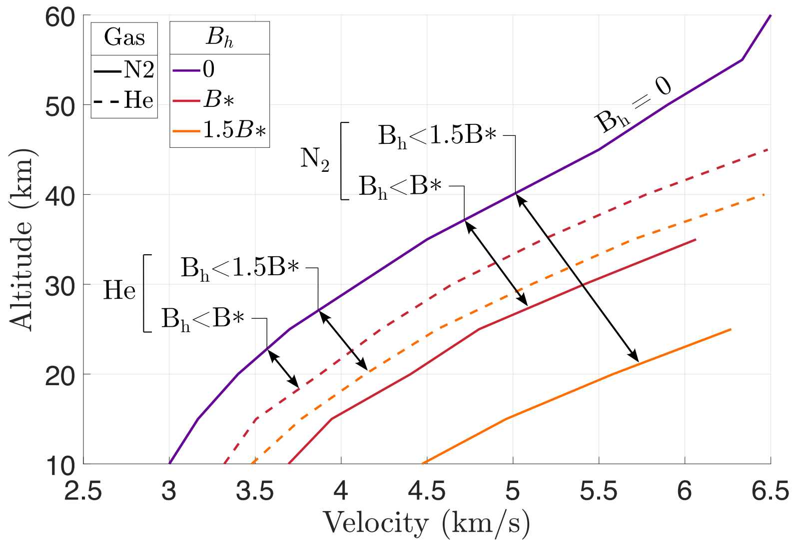


**Fig 14.** Effect of varying coolant. Material: tungsten, $R_{LE}$ = 3 mm.

### *Effect of radius*

Comparing 1 mm and 3 mm tungsten leading edges in Figure 15, the radius of the leading edge has a two-fold effect. The incident heat flux onto the actively cooled is system is higher, so the $B_h/B*$ required for a given condition is lower. However, as velocity increases, the difference in $B_h/B*$ reduces between the two radii. As radius increases, the passively cooled system also experiences lower heat fluxes, so can survive at higher velocities. This means that the band where transpiration cooling may be employed shifts to higher velocities, but doesn't necessarily broaden. Obviously, the increase in radius is associated with aerodynamic penalties that are taken into account during a vehicle design.The internal geometries and plenum pressures of points 1-3 marked in Figure 15 are shown in Figure 16. The plenums are very similar in overall shape, with small changes in height and plenum radius. Since the stagnation point wall thickness is fixed, stagnation point cooling is controlled by plenum pressure, the only non-geometric optimisation output variable. This plenum pressure must increase with stagnation pressure (to overcome the porous pressure gradient), and heat flux (to provide sufficient cooling). For the line $B_h = B*$, the points chosen are within 15% of each other in heat flux, so external pressure is the primary driver toward the large changes in plenum pressure. It may be that higher altitudes correspond to a taller and more rounded plenum, due to the relative change in influence from external pressure to heat flux. Heat flux magnitude does not change as severely as pressure over the surface, and may be further smoothed by lateral conduction within the porous matrix, leading to higher internal radius.

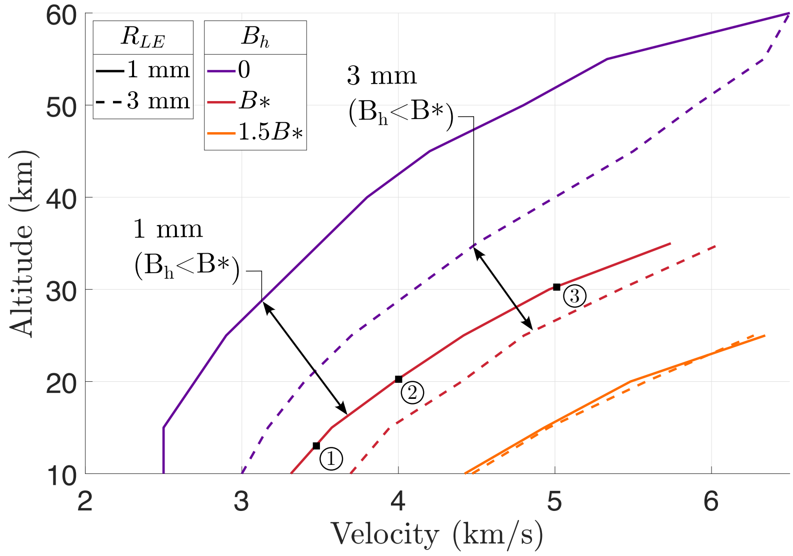


**Fig 15.** Effect of varying radius. Material: tungsten, coolant: nitrogen.

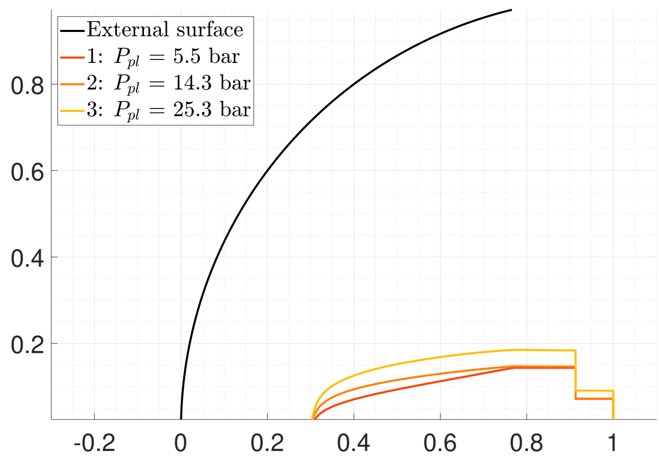


**Fig 16.** Optimised steady-state internal geometries for a 1 mm tungsten leading edge operating with nitrogen at $B_h = B*$ at different flight conditions.

## 5. Conclusions

A numerical tool was developed in *COMSOL Multiphysics* to assess the benefit of transpiration cooling for sharp leading edges in steady flight. The tool takes flight condition, material and geometry inputs to calculate the minimum mass flux distribution needed to cool the leading edge to a target temperature, using empirical correlations applied as boundary conditions to a finite element model. The tool calculates the coupled porous flow and heat transfer processes that describe the temperature response of the material. The mass flux distribution is controlled by means of an optimisation algorithm to calculate the internal geometry and pressure of a single-plenum leading edge with isotropic permeability.

Envelopes where transpiration cooling may be employed were found by running the solver over a series of flight conditions, and comparing the results with a passively cooled ceramic matrix carbon leading edge, as well as considering the upper limits of mass injection. The envelope was extended through choice of heavier gases and high temperature materials. Larger radii allow operation into higher velocity regimes, but do not broaden the range of conditions where transpiration cooling is seen as beneficial.

Work is required to validate the solver against experimental data, which has been carried out in similar studies [25]. Further work is needed on improving the constraints of geometry construction, such that high $B_h$ values can be avoided. The effect of $h_v$ has not been fully explored, and a sensitivity analysis of the material and gas properties may help to improve selection of these design variables. Finally, this work can be expanded to consider a transient trajectory to compare TPS strategies with ablatives, and how a contoured surface operates in the off-design regions of such a trajectory.

## 6. Acknowledgements

*This research was funded and supported by DSTL.*

## References


[1] Takashima, N.: Optimization of waverider-based hypersonic vehicle designs. Ph.D. thesis (1997)

[2] Ohlhorst, C., Glass, D., Bruce, W., Lindell, M., Vaughn, W., Smith, R., Dirling Jr, R., Hogenson, P., Nichols, J., Thompson, D., Kowbel, W., Sullivan, B., Koenig, J.: Development Of X-43A Mach 10 Leading Edges. 56th International Astronautical Congress. Fukuoka, Japan (Oct 17, 2005)

[3] Santos, W.F.N.: Bluntness Impact on Lift-to-Drag Ratio of Hypersonic Wedge Flow. Journal of Spacecraft and Rockets, 46(2):329–339 (2009). URL http://dx.doi.org/10.2514/1.41387

[4] Reuther, J., Kinney, D., Smith, S., Kontinos, D., Gage, P., Saunders, D.: A reusable space vehicle design study exploring sharp leading edges. AIAA Thermophysics Conference. American Institute of Aeronautics and Astronautics., Anaheim, CA; United States; (Jun 11, 2001). URL http://dx.doi.org/10.2514/6.2001-2884

[5] Wright, M., Dec, J.: Aerothermodynamic and Thermal Protection System Aspects of Entry System Design Workshop. Thermal and Fluids Analysis Workshop. National Aeronautics and Space Administration, Pasadena, California (August 13-17, 2012)

[6] Hunter, D.: UK Hypersonic Glide Vehicle Concept and Performance Assessment. Tech. rep., Ministry of Defence (2019). Report No. Dstl/CP119192

[7] Laub, B., Venkatapathy, E.: Thermal protection system technology and facility needs for demanding future planetary missions. A. Wilson, editor, Planetary Probe Atmospheric Entry and Descent Trajectory Analysis and Science, vol. 544 of ESA Special Publication, pp. 239–247 (2004)

[8] Williams, S.D., Curry, D.M.: Assessing the orbiter thermal environment using flight data. Journal of Spacecraft and Rockets, 21(6):534–541 (1984). URL http://dx.doi.org/10.2514/3.25692

[9] Wright, M.J., Beck, R.A.S., Edquist, K.T., Driver, D., Sepka, S.A., Slimko, E.M., Willcockson, W.H.: Sizing and Margins Assessment of Mars Science Laboratory Aeroshell Thermal Protection System. Journal of Spacecraft and Rockets, 51(4):1125–1138 (2014). URL http://dx.doi.org/10.2514/1.A32579

[10] Milos, F.S.: Galileo Probe Heat Shield Ablation Experiment. Journal of Spacecraft and Rockets, 34(6):705–713 (1997). URL http://dx.doi.org/10.2514/2.3293

[11] Glass, D.: Ceramic Matrix Composite (CMC) Thermal Protection Systems (TPS) and Hot Structures for Hypersonic Vehicles. 15th AIAA International Space Planes and Hypersonic Systems and Technologies Conference. Dayton, OH, USA (2008). URL http://dx.doi.org/10.2514/6.2008-2682

[12] Cresci, R.J.: Theoretical analysis of the downstream influence of mass transfer in a stagnation region. International Journal of Heat and Mass Transfer, 5(9):837–857 (1962). URL http://dx.doi.org/10.1016/0017-9310(62)90183-7

[13] Yoshikawa, K.K.: Linearized theory of stagnation point heat and mass transfer at hypersonic speeds. Tech. rep., NASA Ames Research Centre (1971). Report No. NASA-TN-D-6262

[14] Ewenz Rocher, M., Hermann, T., McGilvray, M., Gollan, R.: Correlation for Species Concentration on a Hypersonic Stagnation Point with Mass Injection. AIAA journal, 60(5):2798–2809 (2022). URL http://dx.doi.org/10.2514/1.J061159

[15] Ifti, H.S., Hermann, T., Ewenz Rocher, M., Doherty, L., Hambidge, C., McGilvray, M., Vandeperre, L.: Laminar transpiration cooling experiments in hypersonic flow. Experiments in Fluids, 63(6):102 (2022). URL http://dx.doi.org/10.1007/s00348-022-03446-1

[16] Naved, I., Hermann, T., Hambidge, C., Saad Ifti, H., Falsetti, C., McGilvray, M., Tirichenko, I.S., Vandeperre, L.: Transpiration-Cooling Heat Transfer Experiments in Laminar and Turbulent Hypersonic Flows. Journal of Thermophysics and Heat Transfer (2022). URL http://dx.doi.org/10.2514/1.T6626

[17] Pappas, C.C., Lee, G.: Heat transfer and pressure on a hypersonic blunt cone with mass addition. AIAA Journal, 8(5):954–956 (1970). URL http://dx.doi.org/10.2514/3.5801

[18] Dunavant, J.C., Everhart, P.E.: Explorator heat-transfer measurements at Mach 10 on a 7.5 deg total-angle cone downstream of a region of air and helium transpiration cooling. Tech. rep., National Aeronautics and Space Administration (1969). Report No. NASA-TN-D-5554

[19] Swann, R.T., Pittman, C.M.: Numerical Analysis of the Transient Response of Advanced Thermal Protection Systems for Atmospheric Entry. Tech. rep., National Aeronautics and Space Administration (1962). Report No. NASA-TN-D-1370

[20] Naved, I., Hermann, T., McGilvray, M., Ewenz Rocher, M., Hambidge, C., Doherty, L., Le Page, L., Grossman, M., Vandeperre, L.: Heat Transfer Measurements of a Transpiration-Cooled Stagnation Point in Transient Hypersonic Flow. Journal of Thermophysics and Heat Transfer (2022). URL http://dx.doi.org/10.2514/1.T6610

[21] Brody, S., Lau, K.S., Clarke, J., McGilvray, M., Luca, D.M.: Numerical Simulation of Transpiration Cooling on Stagnation Line in Thermochemical Non-Equilibrium. AIAA SCITECH 2024 Forum. American Institute of Aeronautics and Astronautics (2024). 20; M1: 0; doi:10.2514/6.2024-0648

[22] Ravichandran, R., Doherty, L.J., McGilvray, M., Damm, K., Gollan, R.: Aerodynamic Effects and Heat Flux Augmentation of a Transpiration Cooled Hypersonic Sharp Leading Edge. American Institute of Aeronautics and Astronautics, National Harbor, MD, USA (2023). URL http://dx.doi.org/10.2514/6.2023-0437

[23] Böhrk, H., Piol, O., Kuhn, M.: Heat Balance of a Transpiration-Cooled Heat Shield. Journal of Thermophysics and Heat Transfer, 24(3):581–588 (2010). URL http://dx.doi.org/10.2514/1.47172

[24] Böhrk, H., Dittert, C., Weihs, H., Thiele, T., Gülhan, A.: Sharp Leading Edge at Hypersonic Flight: Modeling and Flight Measurement. Journal of Spacecraft and Rockets, 51(5):1753–1760 (2014). URL http://dx.doi.org/10.2514/1.A32892

[25] Hermann, T., Naved, I., McGilvray, M.: Tool for Rapid Transient Transpiration-Cooled Reentry Simulation. AIAA Journal, 58(2):842–853 (2020). URL http://dx.doi.org/10.2514/1.J058516

[26] Hermann, T., McGilvray, M., Naved, I.: Performance of Transpiration-Cooled Heat Shields for Reentry Vehicles. AIAA Journal, 58(2):830–841 (2020). URL http://dx.doi.org/10.2514/1.J058515

[27] Gordon, S., MacBride, B.J.: Computer program for calculation of complex chemical equilibrium - I. Analysis. Tech. rep., National Aeronautics and Space Administration (1996). Report No. NASA-RP-1311

[28] Gordon, S., MacBride, B.J.: Computer Program for Calculation of Complex Chemical Equilibrium Compositions and Applications - II. User's Manual and Program Description. Tech. rep., National Aeronautics and Space Administration (1996). Report No. NASA-RP-1311-P2

[29] Fay, J.A., Riddell, F.R.: Theory of Stagnation Point Heat Transfer in Dissociated Air. Journal of the Aerospace Sciences, 25(2):73–85 (1958). URL http://dx.doi.org/10.2514/8.7517

[30] Crabtree, L.F., Woodley, J.G., Dommett, R.L.: Estimation of Heat Transfer to Flat Plates, Cones and Blunt Bodies. Tech. rep., Aeronautical Research Council, Ministry of Technology (1970). Report No. Reports and Memoranda No. 3637

[31] Lees, L.: Laminar Heat Transfer Over Blunt-Nosed Bodies at Hypersonic Flight Speeds. Journal of Jet Propulsion, 26(4):259–269 (1956). URL http://dx.doi.org/10.2514/8.6977

[32] The MathWorks Inc.: Global Optimisation Toolbox: Particle Swarm Options (2024). Available from: https://uk.mathworks.com/help/gads/particle-swarm-options.html. Accessed on 20/03/2024

[33] Ifti, H.S., Hermann, T., McGilvray, M.: Flow Characterisation of Transpiring Porous Media for Hypersonic Vehicles. The American Institute of Aeronautics and Astronautics, Orlando, Florida (2018). URL http://dx.doi.org/10.2514/6.2018-5167

[34] Chakravarthy, K.: Multiparameter optical diagnostics for high-speed flow applications. Ph.D. thesis, University of Oxford (2021)

[35] C. Selcuk, N.M., Wood, J.V.: Porous tungsten with controlled porosity by low temperature sintering. Powder Metallurgy, 48(1):17–22 (2005). URL http://dx.doi.org/10.1179/003258905X37648

[36] COMSOL Inc: Material Library User's Guide (2024). Available from: https://doc.comsol.com/6.1/doc/com.comsol.help.matlib/MaterialLibraryUsersGuide.pdf and https://www.comsol.com/material-library. Accessed on 20/03/2024

[37] Fusaro, R., Ferretto, D., Viola, N., Scigliano, R., De Simone, V., Marini, M.: Liquid Metals Heat-Pipe solution for hypersonic air-intake leading edge: Conceptual design, numerical analysis and verification. Acta Astronautica, 197:336–352 (2022). URL http://dx.doi.org/https://doi.org/10.1016/j.actaastro.2022.05.034

[38] Gülhan, A., Braun, S.: An experimental study on the efficiency of transpiration cooling in laminar and turbulent hypersonic flows. Experiments in fluids, 50(3):509–525 (2010). URL http://dx.doi.org/10.1007/s00348-010-0945-6